JOURNAL OF GEOPHYSICAL RESEARCH: OCEANS, VOL. 118, 1302–1315, doi:10.1002/jgrc.20129, 2013

# Low-frequency sea level variability in the southern Indian Ocean and its impacts on the oceanic meridional transports

Wei Zhuang,[1] Ming Feng,[2] Yan Du,[1] Andreas Schiller,[3] and Dongxiao Wang[1]

Received 20 August 2012; revised 9 February 2013; accepted 13 February 2013; published 18 March 2013.

[1] Sea levels in the southern Indian Ocean (SIO) display significant interannual to decadal variability. Off the northwest Australian coast, it has been demonstrated that sea level variability is mostly modulated by remote wind forcing from the tropical Pacific through equatorial and coastal waveguides. In this study, a linear reduced gravity model is used to investigate relative contributions of local wind forcing and remote forcing from the Pacific to the sea level variability of the SIO, with a focus on the western SIO. North of the South Equatorial Current bifurcation latitude (17ºS), model simulated sea levels are well correlated with altimeter observations at the dissipation timescale of about 3 years, suggesting that sea level variability on interannual-to-decadal timescales could well be explained by nondispersive baroclinic Rossby wave adjustment. The large sea level variability of the western SIO is primarily caused by westward-propagating Rossby waves driven by wind stress curl in 70°E-95°E, with a minor influence from the remote Pacific forcing. To the south, sea level variability at around 20ºS displays lower amplitude due to weaker wind variations at this latitude band, and the modeled sea level variability is weaker than observations. There is a close linkage between the cross-basin sea level difference at 15ºS and the interior meridional ocean transport across this latitude on decadal timescales, as assessed with outputs from a data-assimilation model. Thus, the meridional overturning cell of the SIO is influenced by both remote forcing from equatorial Pacific and local winds in the SIO.

**Citation:** Zhuang, W., M. Feng, Y. Du, A. Schiller, and D. Wang (2013), Low-frequency sea level variability in the southern Indian Ocean and its impacts on the oceanic meridional transports, *J. Geophys. Res. Oceans*, *118*, 1302–1315, doi:10.1002/jgrc.20129.

## 1. Introduction

[2] The South Indian Ocean (SIO) is bounded by the African coast to the west and by Sumatra, Java, and the Western Australian coast to the east and connects to the Southern Ocean to the south. North of 10ºS in the SIO, the wind climate is dominated by the monsoon system, with northeasterly winds blowing from November to March and southwesterly winds from May to September [*Schott and McCreary*, 2001]. The southeast trades prevail over the region between 10ºS–30ºS (Figure 1a). The peak easterly trade wind occurs at the latitude of ~17ºS in the interior basin, resulting in negative wind stress curl (WSC) to the north and positive WSC to the south.

[3] The WSC forcing is reflected in the mean geostrophic flow of the tropical and subtropical gyres and a westward intergyre flow, the South Equatorial Current (SEC, see Figure 1b). As a band of flow between 10ºS–20ºS extending across the SIO basin, the SEC is to a large part supplied by the Indonesian Throughflow (ITF) in the eastern basin and modulated by the local trade winds during its westward movement [*Qu and Meyers*, 2005; *Zhou et al.*, 2008]. Upon reaching the east coast of Madagascar Island, the SEC bifurcates at about 17ºS into two western boundary branches [*Schott et al.*, 2009]. The northward branch flows toward the eastern African coast and further splits into the southward current in the Mozambique Channel and the northward Eastern African Coastal Current. The southward branch forms active eddies south of 20ºS [*Quartly et al.*, 2006] and partly retroflects to supply the northeastward South Indian Countercurrent (SICC).

[4] Sea level in the SIO displays pronounced variability at interannual and decadal timescales [*Masumoto and Meyers*, 1998; *Chambers et al.*, 1999; *Birol and Morrow*, 2001; *Wijffels and Meyers*, 2004; *Lee and McPhaden*, 2008; *Feng et al.*, 2010; *Han et al.*, 2010; *Trenary and Han*, 2012] and the spatially nonuniform sea level variations indicate changes in the SIO circulation. In the past two decades, the global averaged sea surface height (SSH) has risen at a mean rate of ~ 3 mm/yr [e.g., *Church et al.*, 2004]; however, in the

[1]State Key Laboratory of Tropical Oceanography, South China Sea Institute of Oceanology, Chinese Academy of Sciences, Guangzhou, China.
[2]CSIRO Marine and Atmospheric Research, Floreat, Western Australia, Australia.
[3]CSIRO Marine and Atmospheric Research, Hobart, Tasmania, Australia.

Corresponding author: W. Zhuang, LTO, South China Sea Institute of Oceanology, 164 West Xingang Road, Guangzhou, 510301, China. (zhuang@scsio.ac.cn)


2169-9275/13/10.1002/jgrc.20129

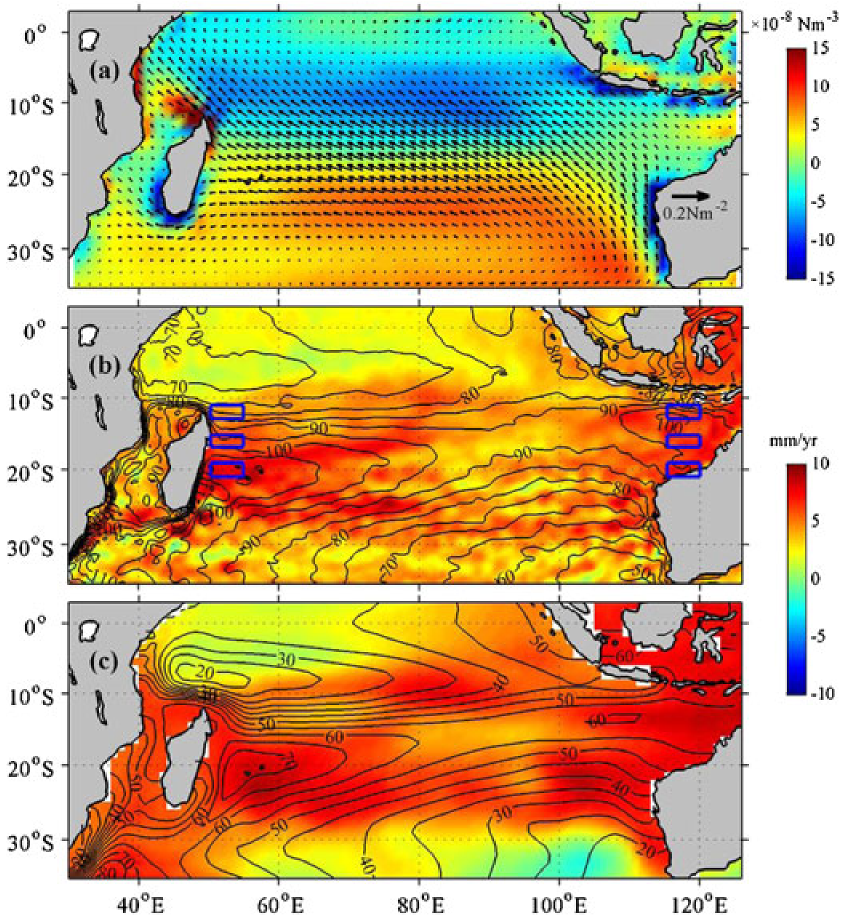


**Figure 1.** (a) Climatological ECMWF interim annual mean wind stress (N/m$^2$, vectors) and wind stress curl ($\times 10^{-8}$ N/m$^3$, shading). (b) Mean SSH (cm, contour) from *Rio et al*. [2011] and linear trend of altimetric sea level in 1993–2009 (mm/year, shading). (c) The same as Figure 1b, but from ECMWF ORA-S3 reanalysis data in 1993–2009.

broad regions of SIO, the SSH rise trend exceeds 5 mm/yr. The most significant rise (> 7 mm/yr) occurs near the eastern and western boundaries of extra-equatorial SIO (Figure 1b).

[5] Recent studies suggested that the interannual-to-decadal sea level variations in the SIO are in response to the variability of large-scale atmospheric circulations over both the Pacific and Indian Ocean (IO) [*Wijffels and Meyers*, 2004; *Feng et al*., 2010; *Han et al*., 2010; *Schwarzkopf and Böning*, 2011]. Locally, the negative WSC between the southeast trades and equatorial westerlies drives open ocean upwelling and forms a thermocline ridge in the southwestern tropical IO [*McCreary et al*., 1993; *Yokoi et al*., 2008]. In this upwelling zone, the thermocline depth variability has a strong influence on sea surface temperature (SST), which further exerts significant impacts on the local atmospheric convection and remote climate variability [e.g. *Xie et al*., 2002; *Bader and Latif*, 2003; *Hoerling et al*., 2004; *Du et al*., 2009; *Xie et al*., 2009]. Unlike the eastern Pacific and Atlantic, unusually high sea level variability is evidenced in the eastern basin of SIO, due to the intersection of the Pacific and IO wave guides at the Indonesian Archipelago and a pathway for signals generated in the tropical Pacific to enter the SIO [*Potemra*, 2001; *Feng et al*., 2004; *Wijffels and Meyers*, 2004; *Feng et al*., 2010]. After reaching the southeast tropical IO, the coastally trapped Kelvin waves can radiate westward as Rossby waves into the interior SIO basin and impact SSH and upper ocean heat content [*Verschell et al*., 1995; *Masumoto and Meyers*, 1998; *Birol and Morrow*, 2001; *Wijffels and Meyers*, 2004; *Trenary and Han*, 2012]. In addition, the ITF may also influence the SIO water mass characteristics through heat and salt advections [e.g., *Gordon and Fine*, 1996; *Du and Qu*, 2010].

[6] Previous studies have investigated the relative importance of the local wind forcing and remote Pacific forcing to the SSH and thermocline changes in the low latitude SIO. Numerical experiments by *Verschell et al*. [1995] suggested that the wave transmissions through the Indonesian Archipelago deepen the mean IO thermocline by 14% and mainly enhance thermocline variability around 14ºS at periods longer than $\frac{1}{2}$ year. Whereas, utilizing altimeter and expendable bathythermograph (XBT) observations, *Wijffels and Meyers* [2004] found that the interannual wave signals from Pacific dominates much of the thermocline variability in the southeast IO and weakens significantly near 100ºE. The synergy of XBT profiles and model simulations indicated that local wind forcing strongly modifies Rossby waves radiating from the eastern boundary and dominates the seasonal and interannual thermocline variability in the

interior SIO [*Masumoto and Meyers*, 1998]. *Birol and Morrow* [2001] also supported the dominance of local wind to the SSH variability in the SIO and further noted that the signals radiating from the eastern boundary seem to be important to explain the observed variability east of 90ºE. *Trenary and Han* [2012] provided more systematic investigations of local versus remote forcing on SSH variability around the SIO thermocline ridge (50ºE–80ºE, 5ºS–12ºS). They found that the seasonal-to-interannual SSH variability over the thermocline ridge is dominated by local wind-driven Ekman pumping and westward-propagating Rossby waves, while the remote Pacific forcing has weak impact. Another interesting phenomenon is that to the south of 23ºS, the interannual coastal signals are trapped by the Leeuwin Current and could hardly propagate westward as Rossby waves [*Clarke and Li*, 2004]. This region displays notable westward-propagating mesoscale eddies generated by the instabilities of interior and boundary flows [e.g., *Morrow et al*., 2003; *Rennie et al*., 2007; *Jia et al*., 2011].

[7] On the decadal to multidecadal timescales, large-scale sea levels decreased substantially in the south tropical IO but increased in the subtropical from 1960s to 1990s [*Han et al*., 2010; *Timmermann et al*., 2010; *Schwarzkopf and Böning*, 2011], which accompanied the tropical cooling and subtropical warming in subsurface ocean, respectively [*Han et al*., 2006; *Alory et al*., 2007; *Du and Xie*, 2008]. Several mechanisms have been brought forward to explain this pattern. Results from simplified layer models suggested that the regional features of recent decadal and multidecadal sea level trends in the SIO can be attributed to wind-driven anomalous Ekman Pumping over the SIO [*Han et al*., 2006; *Timmermann et al*., 2010], which is associated with the changes in the large-scale prevailing wind regimes over this region [*Han et al*., 2010]. In contrast, the simulation and numerical experiments of a global ocean model indicated that in the SIO, interannual variability appears mainly governed by local atmospheric forcing, while multidecadal changes also involve a significant contribution from the western Pacific via wave transmission through the Indonesian Archipelago [*Schwarzkopf and Böning*, 2011].

[8] The decadal to multidecadal SSH changes are closely related to the IO meridional overturning circulation, also called subtropical cell (STC), which is assumed to be quasi-steady on decadal or longer timescales [*McCreary and Lu*, 1994; *Lee*, 2004; *Trenary and Han*, 2008]. The STC in the IO consists of the southern STC (SSTC) and Cross-Equatorial Cell (CEC), as conceptually shown in Figure 1 of *Lee* [2004]. Both cells transport the surface warm water southward and colder thermocline water northward. To the north of 10ºS, the surface and lower branches of CEC and STC are mainly connected by the upwelling in the northern IO and near the SIO thermocline ridge, respectively [*Lee and Marotzke*, 1998; *Schott et al*., 2004]. The surface branch of STC is largely controlled by the zonal wind stress at the latitude 10ºS–20ºS band [*McCreary and Lu*, 1994; *Trenary and Han*, 2008], while the lower branch, supplied by southern subduction, recirculation and inflow from the ITF [*Schott et al*., 2004], could be inferred from SSH differences across the SIO basin under geostrophic approximation [*Lee*, 2004; *Lee and McPhaden*, 2008]. During 1961–2000, the multidecadal sea level decrease and subsurface cooling around the SIO thermocline ridge are consistent with the intensification of SSTC [*Trenary and Han*, 2008]. On decadal timescales, satellite altimeter observations indicate a slowdown of the IO STC for the period 1992–2000 and a rebound during 2000–2006 [*Lee*, 2004; *Lee and McPhaden*, 2008].

[9] While previous studies tried to examine the roles of IO and Pacific forcing on the SIO sea level changes, systematic investigations of their relative importance have only been provided around the SIO thermocline ridge by *Trenary and Han* [2012]. Specifically, the features and dynamic mechanisms of the SSH variability near the western boundary of SIO in the latitude band of 10ºS–20ºS (named $H_w$) have not yet been well illustrated. Considering the potential impacts of $H_w$ on the variability of STC strength, the present study aims to further quantify the respective contributions of local SIO and remote Pacific wind forcing to the low-frequency $H_w$ variability, with the synergy of observations and a 1½-layer baroclinic Rossby wave model. Here, low-frequency variability is defined as variability with periods longer than 13 months and high-frequency variability as periods shorter than 13 months. Utilizing a global ocean data-assimilation model, we further verify the relationship between cross-basin SSH difference and the transports within STC lower branch, which is speculated to follow the geostrophy on decadal and longer timescales [e.g., *Lee*, 2004]. The thermosteric and halosteric effects to the linear sea level trend over the 1993–2009 period are also discussed based on the 4-D output from the global ocean model.

[10] The organization of this paper is as follows. Section 2 introduces the observational data, the linear Rossby wave model, and the global data-assimilation model. Section 3 describes the spatiotemporal variations of SSH and explores the relative importance of the interior IO forcing versus the remote forcing from the Pacific. Based on the global ocean model simulations, Section 4 investigates the ocean vertical structure associated with the sea level trends and the relationship between SSH and oceanic transports. Section 5 is a summary and discussion.

## 2. Data and Method

### 2.1. Altimeter Data

[11] In this study, we use a gridded sea level anomalies (SLA) data set from multisatellite altimeters, which is distributed by the Collecte Localisation Satellites (CLS) Space Oceanographic Division of Toulouse, France. To keep the sampling resolution of the total series homogeneous, we adopt the merged SLA data derived from simultaneous measurements of two satellites (Topex/Poseidon or Jason-1/2 + ERS or Envisat). The merged data set provides more realistic SLA and geostrophic velocity statistics than any individual data set [*Ducet et al*., 2000]. The product is available on 1/3° Mercator spatial resolution and covers the period from October 1992 to December 2010. Because the focus of the present study is on the low-frequency sea level variations, the original weekly data are temporally averaged to form a monthly SLA data set.

### 2.2. The Baroclinic Rossby Wave Model

[12] In extra-equatorial regions, large-scale sea level variations in the open ocean can be largely explained by the westward propagating Rossby waves either driven by wind-induced Ekman pumping and/or radiated from the

eastern boundary [*Meyers*, 1979; *Masumoto and Meyers*, 1998]. Under the long-wave approximation, these processes can be quantified by a 1½-layer reduced-gravity model [e.g., *Capotondi and Alexander*, 2001; *Qiu*, 2002], which is governed by the following linear vorticity equation:

$$\frac{\partial h}{\partial t} - c_R \frac{\partial h}{\partial x} = -\frac{g' \nabla \times \tau}{\rho_0 g f} - \varepsilon h, \tag{1}$$

where $h$ is baroclinic component of the SLA, $c_R$ the zonal phase speed of the long baroclinic Rossby wave, $g$ the gravitational constant, $g'$ the reduced gravity, $\tau$ the anomalous wind stress vector, $\rho_0$ the density, $f$ the Coriolis parameter, and $\varepsilon$ the Newtonian damping coefficient. Integrating equation (1) westward from the eastern boundary ($x_e$) yields the solution:

$$\begin{aligned} h(x,y,t) &= h\left(x_e, y, t + \frac{x - x_e}{c_R}\right) \exp\left[\frac{\varepsilon}{c_R}(x - x_e)\right] \\ &+ \frac{1}{\rho_0 g f} \int_{x_e}^{x} \frac{g'}{c_R} \nabla \times \tau\left(x', y, t + \frac{x - x'}{c_R}\right) \\ &\exp\left[\frac{\varepsilon}{c_R}\left(x - x'\right)\right] dx'. \end{aligned} \tag{2}$$

[13] The first and second terms on the right-hand side of equation (2) represent SSH signals radiated from the eastern boundary and induced by interior wind forcing, respectively. To evaluate the low-frequency SSH variability, we calculate monthly mean wind stresses by averaging the six-hourly European Center for Medium-Range Weather Forecasts (ECMWF) ERA-interim data. ERA-interim is the latest global atmospheric reanalysis produced by the ECMWF (available at http://data-portal.ecmwf.int/data/d/interim_daily/). The horizontal resolution of the surface wind product is 1.5º × 1.5º. The phase speed $c_R$ is generally based on the values derived by *Chelton et al.* [1998] and corrected slightly at some latitudinal bands based on the altimetric observations. Compared with the $c_R$ determined by the standard long Rossby wave theory [*Chelton et al.*, 1998], the altimetric observations are almost the same at 14ºS–18ºS but exhibit zonal mean biases of 2–4 cm/s slower to the northward (10ºS–13ºS) and faster southward (19ºS–22ºS), respectively. The $g'$ values are estimated from $g' = \frac{c_g^2}{H_t}$, where $c_g$ is the baroclinic gravity-wave phase speed from *Chelton et al.* [1998] and $H_t$ is the thermocline depth defined as the 20°C isotherm depth in World Ocean Atlas data set. The zonal mean $g'$ within the SIO varies from 0.052 m/s$^2$ at 20ºS to 0.071 m/s$^2$ at 10ºS. *Qiu* [2002] showed the necessity to include the dissipation to match the solution to observations. We therefore choose a wide range of the $\varepsilon$ values to minimize the discrepancies between the model simulations and observations. As the seasonal SSH signals can be significantly affected by other factors (e.g., seasonal surface heat fluxes) [*Vivier et al.*, 1999; *Bowen et al.*, 2006], the optimal $\varepsilon = (3\,\text{yr})^{-1}$ for the latitudes of 10ºS–22ºS is determined by the low-frequency signals, which are also the focus of this study. Note that choosing an $\varepsilon$ value in the range from $(2\,\text{yr})^{-1}$ to $(5\,\text{yr})^{-1}$ does not alter the model's predictive skill significantly. Along the eastern boundary, $h(x_e, y, t)$ is determined by the monthly altimetric SLA with the removal of 3 mm/yr global sea level trend. Given that $\varepsilon$ near the coast or over the shallow shelf is usually stronger due to topographic scattering and the vertical propagation of wave energy [*Kessler and McCreary*, 1993], we select the location of $x_e$ in the open ocean west of the shallow shelves with water depth > 1000 m instead of strictly close to the coast. Therefore, the dissipation rate associated with the boundary-forced signals could be approximately equal to the value associated with the interior wind-driven signals.

### 2.3. ECMWF Ocean Analysis System ORA-S3

[14] ORA-S3 is an operational ocean analysis/reanalysis system being implemented at ECMWF based on the Hamburg Ocean Primitive Equation model [*Wolff et al.*, 1997] and the optimal interpolation assimilation scheme. ORA-S3 assimilates the in situ temperature and salinity profiles, altimeter-derived sea level anomalies and global sea level trends, and the velocity corrections are derived from the assimilation increments in the temperature and salinity imposing geostrophic balance. It is designed to reduce spurious climate variability in the resulting ocean reanalysis due to the nonstationary nature of the observing system, while still taking advantage of the observations information [*Balmaseda et al.*, 2008]. *Balmaseda et al.* [2008] compared the ORA-S3 analysis with the previous operational version and found that it not only improves the fit to the data but also improves the representation of the interannual variability. The data at the resolution of 1º × 1º during 1959–2009 are available on Asia-Pacific Data-Research Center (APDRC), University of Hawaii and used in this study.

## 3. Low-Frequency Sea Level and Wind Variability

### 3.1. The Observed SSH Variations in the SIO

[15] To capture the large-scale SSH changes in the SIO, we firstly apply the empirical orthogonal function (EOF) analysis to the altimetric SLA in the region of our interest: 8°S–30°S so that the EOF patterns and the associated principal components (PCs) represent the spatial and temporal variations, respectively. Because we are interested in low-frequency variability, the monthly climatological mean and intraseasonal signals (<3 month) are removed from the original SLA prior to the EOF analysis. The first EOF mode explains 23.0% of the total variance, and its spatial pattern and weighting coefficient are shown in Figure 2. The EOF-1 shows the oppositely signed SLAs to the east and west of ~95°E. In the western basin, large sea level amplitude is primarily found north of 20°S. The PC-1 shows significant interannual to decadal variations. It descends from 1993 to 2000 and then rebounds quickly from 2000 to 2003, consistent with the decadal sea level phase change noted by *Lee and McPhaden* [2008]. A close inspection of the PC-1 hints that there is no significant trend during 2004–2010. In addition, there exist SSH peaks in the end of years 1997, 2002, and 2006, indicative of the impact of El Niño events and co-occurring positive Indian Ocean Dipole.

[16] The second EOF mode accounts for 21.5% of the total variance. The EOF-2 and PC-2, shown in Figure 3, display a basin-wide sea level rise from 1993 to 2010. The most conspicuous rise occurs near the southeastern IO east of 110°E and between 18°S and 25°S in the western basin. Due to the dominance of the linear rising trend in this EOF mode, it is not surprising that the spatial pattern of EOF-2 (Figure 3a)

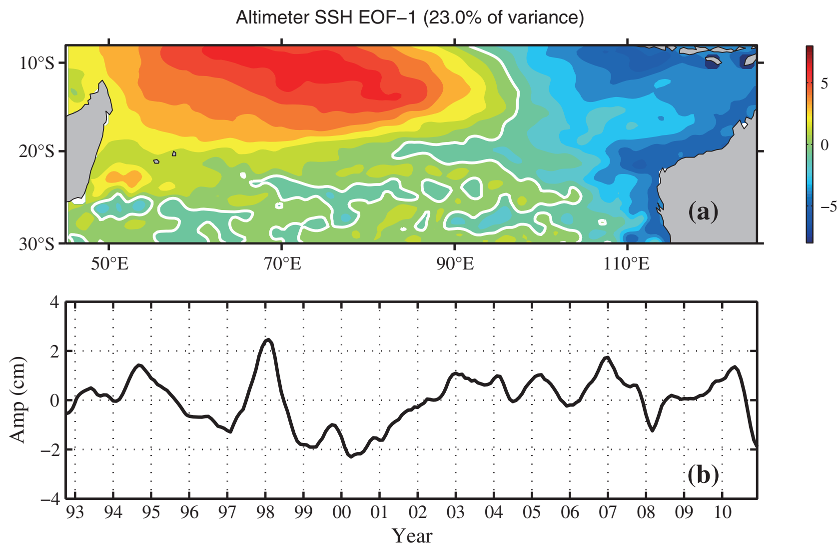


**Figure 2.** (a) EOF-1 and (b) PC-1 of monthly mean SLA for the period October 1992 to December 2010. The climatological seasonal cycle and intraseasonal signals (<3 months) have been removed from the original data before the EOF analysis.

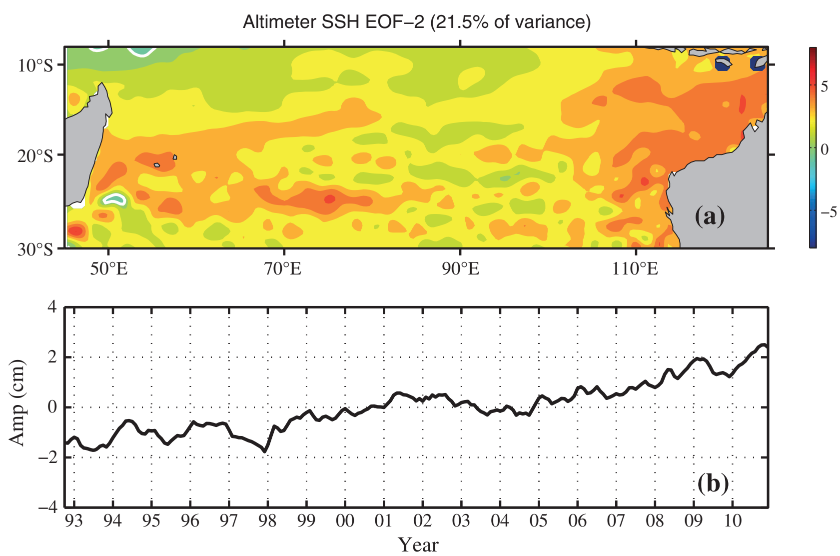


**Figure 3.** (a) EOF-2 and (b) PC-2 of monthly mean SLA for the period October 1992 to December 2010. The climatological seasonal cycle and intraseasonal signals (<3 months) have been removed from the original data before the EOF analysis.

resembles the linear SLA trend pattern presented in Figure 1b. Although the first and second EOF modes explain roughly an equal amount of variance, the fact that the two modes separate the interannual-decadal variations and the linear rise of the sea levels in the SIO suggests that they largely represent two different physical modes. To check the significance of results in Figures 2 and 3, we also applied the EOF analysis to the original monthly altimetric SLA. The new first two EOF modes explain 23.2% and 13.5% of the total variances and similarly display the interannual-decadal variability and linear SSH rise, respectively, with embedded seasonal cycle (not shown). As will be seen below, the interannual-to-decadal signals and linear trends captured in Figures 2 and 3 are both significant in the SIO.

[17] As suggested by *Lee* [2004] and *Lee and McPhaden* [2008], the zonal SSH difference across the SIO basin could be an indicator of the zonal pressure gradient that balances the interior meridional geostrophic flow in the thermocline, which is part of the shallow overturning circulation in the IO. In this study, the low-frequency SLAs near the eastern (115°–120°E) and western (50°–55°E) boundaries of SIO are further illustrated in Figure 4. As indicated in the first and second EOF modes (Figures 2 and 3), sea levels in the western basin exhibit a strong interannual-decadal fluctuation north of 18°S and a significant linear trend around 20°S. Therefore, SLAs are averaged in the six selected boxes at the latitudes 11°–13°S, 15°–17°S, and 19°–21°S (shown in Figure 1b) to make a comparison. The SLAs at the three

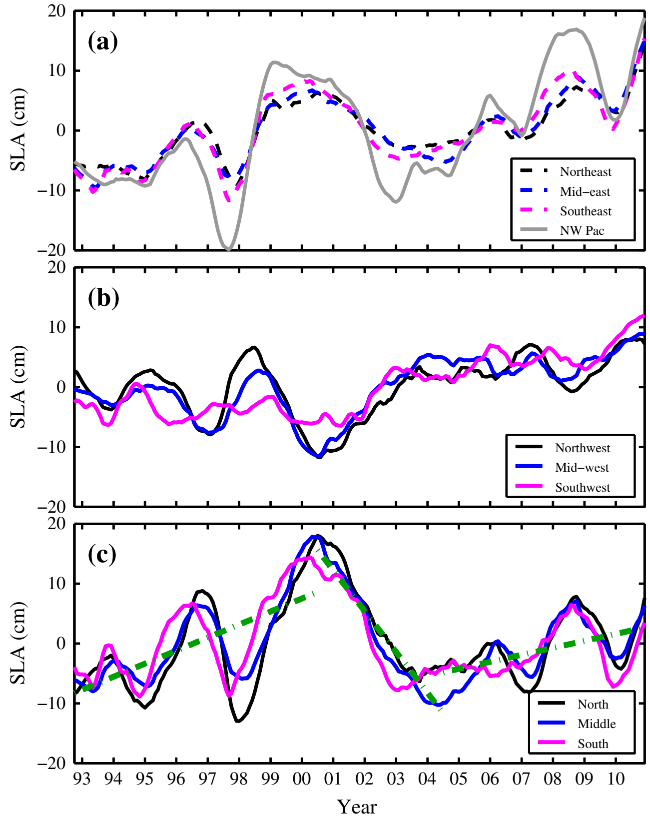


**Figure 4.** Low-frequency (with period > 13 month) altimetric sea level variability near the (a) eastern and (b) western coasts of SIO. (c) SSH differences between the eastern and the western coasts. The sea levels are averaged within the boxes shown in Figure 1. The gray line in (a) indicates the sea level in the Western Pacific (130°E-150°E, 9°N-13°N). The green dashed lines in (c) indicate the linear trends during October 1992 to June 2000, July 2000 to June 2004, and July 2004 to December 2010.

boxes near the eastern coast (named $H_E$) display coherent interannual-decadal variations, which are highly correlated with the sea level fluctuations in the tropical northwestern Pacific (Figure 4a), demonstrating the impact from the tropical Pacific via the coastal Kelvin waveguides around Indonesian Archipelago [e.g., *Wijffels and Meyers*, 2004; *Feng et al.*, 2010]. The amplitude of $H_E$ is relatively large in the southern-most box, compared with the two northern boxes. The northern boxes are further away from the Australian coast (Figure 1) so that the Rossby wave signals radiated from the coastal waveguide are more likely to be modified by WSC during their westward propagations toward the boxes [e.g., *Masumoto and Meyers*, 1998]. Near the western basin, the amplitudes of low-frequency $H_W$ is large north of 18°S and becomes relatively small southward (Figure 4b), consistent with the EOF-1 pattern. The linear $H_W$ rise appears to be more pronounced around 20°S, which is reflected by the EOF-2. It is interesting to note that $H_E$ and $H_W$ tend to be out-of-phase on interannual-decadal timescales, while they both exhibit a linear rise trend in the 1993–2010 period. Therefore, the zonal SSH difference ($H_E$ minus $H_W$) displays large-amplitude low-frequency fluctuations, which under the geostrophic approximation, indicate significant variability of meridional flow and transport in the pycnocline. As shown in Figure 4c, the decadal increasing trend in SSH difference in the 1990s (21.8 mm/yr) changes abruptly to the decrease phase in the 2000–2004 period (-68.1 mm/yr). Afterward, as $H_E$ and $H_W$ both rise steadily, the SSH difference displays a relatively weak increasing trend from 2005 to 2010 (11.7 mm/yr).

### 3.2. Interior Wind Forcing Variability

[18] To understand the role of wind forcing in the SIO, the EOF method is also applied to the WSC of the ECMWF interim product. Similar to Figures 2 and 3, the strong seasonal and intraseasonal monsoon signals are removed from the original WSC data before the EOF analysis. The first EOF mode, as shown in Figure 5, explains 27.5% of the total variance. The largest amplitude of EOF-1 is seen

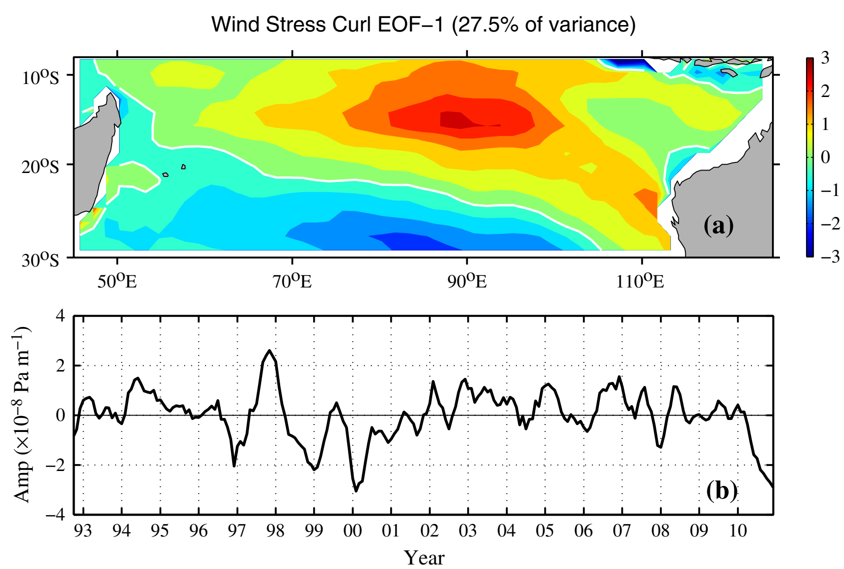


**Figure 5.** (a) EOF-1 and (b) PC-1 of monthly ECMWF interim WSC fields for the period October 1992 to December 2010. The climatological seasonal cycle and intraseasonal signals (<3 months) have been removed from the original data before the EOF analysis.

around 90°E and north of 18°S. The PC-1 for the WSC shows a negative trend over the 1990s, which corresponds to the enhancement of upward Ekman pumping in the 10°S–18°S band (Figure 5a) and a drop in sea level in the western SIO (Figure 4b). The trend in 1990s reverses to be positive since 2000, that is, there is a downward Ekman pumping anomaly north of 18°S, which results in a sea level rebound during 2000–2003. The trend becomes weak in the 2003–2009 period, consistent with the relatively steadiness of sea level variation. The interannual signals associated with ENSO are also clearly shown in the PC-1 of WSC. There are peaks in the end of 1997, 2002, and 2006, which reflect the anticyclonic WSC anomalies induced by El Niño events [e.g., *Xie et al*., 2002; *Yu et al*., 2005] and result in corresponding sea level rise shown in Figure 2.

### 3.3. The Reduced-Gravity Model Simulations

[19] We adopt a 1½-layer linear reduced-gravity model that governs the baroclinic Rossby wave dynamics to further explore the influences of interior wind forcing and the radiation of Rossby waves from the eastern boundary to the SSH changes in the interior SIO. Particular emphasis is placed on the $H_W$ variability. To evaluate the performance of the model, we first compare the observed and modeled $H_W$ variations averaged within the three boxes shown in Figure 1b on interannual-decadal and seasonal timescales, respectively. Considering that the baroclinic Rossby wave model does not capture the sea level rise due to the thermal expansion under a warming climate and the freshwater fluxes from ice-melting, we subtracted the 3 mm/yr global mean sea level rise trend from the observations for a more direct comparison. Since the dissipation rate is a poorly known quantity, we calculate the SSH using different $\varepsilon$ values ranging from 0 (no damping) to $(0.5\,\text{yr})^{-1}$ (strong damping).

[20] At the northern box centered at 12°S, 52.5°E northeast of Madagascar Island, the model well captures the observed low-frequency variations with a correlation coefficient of 0.75 at $\varepsilon = (3\,\text{yr})^{-1}$ (Figure 6a). The model's predictive skill reaches 55.9%. Here the predictive skill is defined according to *Qiu* [2002] as $S = 1 - \left\langle (h_o - h_m)^2 \right\rangle / \left\langle h_o^2 \right\rangle$, where $h_o$ is the observed signal, $h_m$ is the model simulation, and $\langle\ \rangle$denotes the summation over time. At the middle box centered at 16°S, 52.5°E along the mainstream of the SEC (see the MDT in Figure 1b), the modeled low-frequency SSH reaches the best predictive skill (71.8%) and the highest correlation coefficient of 0.85 with the observations at $\varepsilon = (3\,\text{yr})^{-1}$ (Figure 6b). The respective predictive skills for interannual (< 7 yr) and decadal variations (≥7 yr) are 65.6% and 75.5%. Generally, the model is successful in reproducing the interannual to decadal SSH changes observed in the above 2 boxes, including the initial decreasing trend in 1993–2000 and subsequent rising trend in 2000–2003. At the southern box centered at 20°S, 52.5°E located near the center of subtropical gyre, there exist relatively weaker interannual SSH signals and a more conspicuous increasing trend from 1993 to 2010. For this box, the baroclinic Rossby

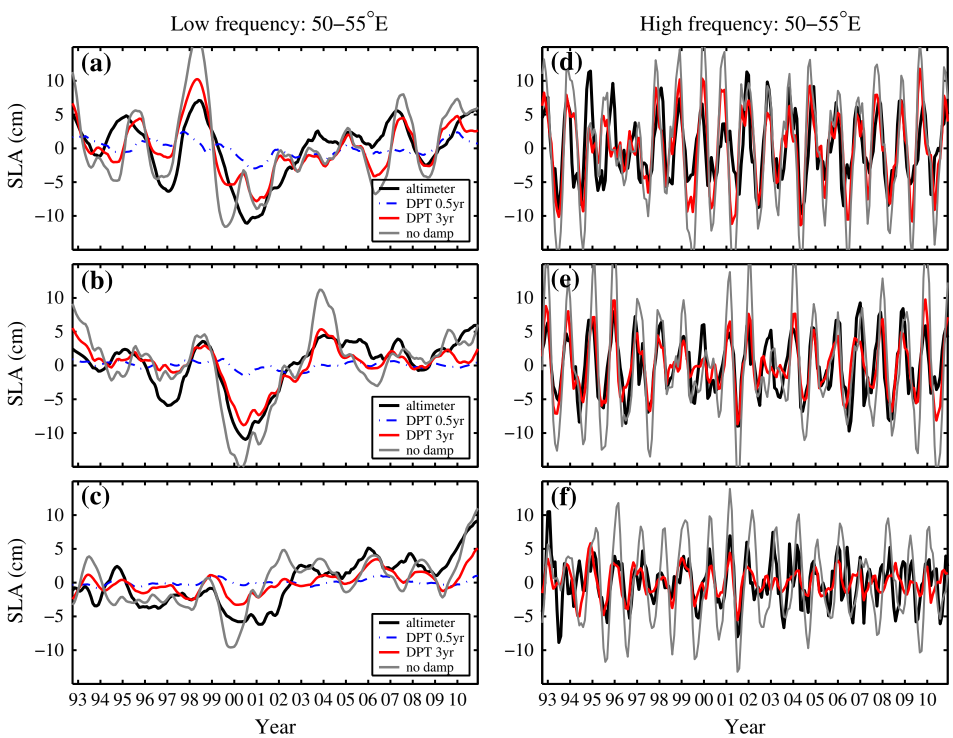


**Figure 6.** Low-frequency variations (with period > 13 month) of altimetric and baroclinic Rossby wave model simulated SLA in (a) northwestern box; (b) middle-west box; (c) southwestern box. (d–f) are similar to (Figures 6a–6c) but for high-frequency variations (with period < 13 month). The boxes are shown in Figure 1b. The red line is the model results with optimal $\varepsilon = (3\,\text{yr})^{-1}$, while the blue and gray lines indicates the model results at $\varepsilon = (0.5\,\text{yr})^{-1}$ and 0, respectively. The results at $\varepsilon = (0.5\,\text{yr})^{-1}$ are not shown in Figures 6d–6f for clarity.

wave model generally captures the phase of observed low-frequency variability with a correlation coefficient of 0.78 at $\varepsilon = (3\,\text{yr})^{-1}$. However, as shown in Figure 6c, the model shows weaker low-frequency SSH amplitude than the observations at $\varepsilon = (3\,\text{yr})^{-1}$, and its predictive skill is relatively low at 50.9%, indicating that other factors aside from baroclinic Rossby wave dynamics would be important. Meanwhile, the high-frequency SSH variations, dominated by the seasonal signals, at these three boxes are partly attributed to the wind-driven baroclinic Rossby wave dynamics. From north to south, the correlation coefficients between observations and simulations could reach 0.65, 0.77, and 0.48 at seasonal timescale (see Figures 6d–6f). In addition, Figure 6 shows when the dissipation rate is extremely large ($\varepsilon^{-1} = 0.5\,\text{yr}$) or small ($\varepsilon^{-1} = +\infty$), the simulations obviously underestimate or overestimate the observed SSH amplitudes within all three boxes, respectively.

[21] To gain a better comparison of the spatiotemporal structures between the observations and model simulations, the time-longitude diagrams of observed and modeled low-frequency SLAs along two typical latitudinal bands are plotted. As shown in Figure 7, the observed and simulated patterns in the 15°S–17°S latitudinal band exhibit favorable correspondence and feature significant westward propagations. The correlation coefficients between the SSH time series from the observations and the model vary gradually from 1.0 at eastern boundary to 0.67 at 91°E and then increase westward slowly to above 0.8 west of 80°E (not shown). Their zonal average correlation reaches 0.84. West of 100°E both the altimeter data and the model output show a decreasing sea level trend prior to year 2000 and an increasing trend thereafter (Figure 7). Similar decadal phase change could also be seen at 11°S–13°S latitudinal band (not shown). Along the 19°S–21°S band, both the observed and simulated patterns show strong interannual-decadal variability near the eastern boundary, which dissipates gradually during its westward propagation (Figure 8). Toward the western basin, due to the relatively weak low-frequency WSC amplitude in the interior basin along ~20°S (see Figure 5), the SSH displays weaker oscillations than those north of 18°S. The zonal mean correlation coefficients between the SSH time series from the observations and the model is 0.77.

### 3.4. Effects of Local Wind and Eastern Boundary Forcing on the Low-Frequency $H_W$

[22] Because the observed $H_W$ could be captured by the baroclinic Rossby wave model, quantifying the contributions of different forcings to the modeled $H_W$ could help us to better understand the dynamics underlying the SSH changes in the southwest IO. As the modeled $H_W$ reflect the cumulative effects of local WSC forcing along the different parts of the SIO basin and the remote Pacific forcing transmitted via the gappy ITF passages, we calculate the $H_W$ variance explained by the cumulative wind forcing as a function of longitude $X$ east of the three key boxes near the western boundary. This method has been effectively used by *Qiu and Chen* [2010] to study the influence of WSC to the North Equatorial Current in the Pacific Ocean. At a latitude band $y_0$, the definition of explained variance is

$$S(X, y_0) = 1 - \left\langle [H_w(t) - h_I(X, y_0, t)]^2 \right\rangle / \left\langle H_w^2(t) \right\rangle \tag{3}$$

where $H_w(t)$ represents the SLA near the western boundary ($x = x_w$) derived from equation (2), which includes the signals forced by the SIO local wind and radiated from the

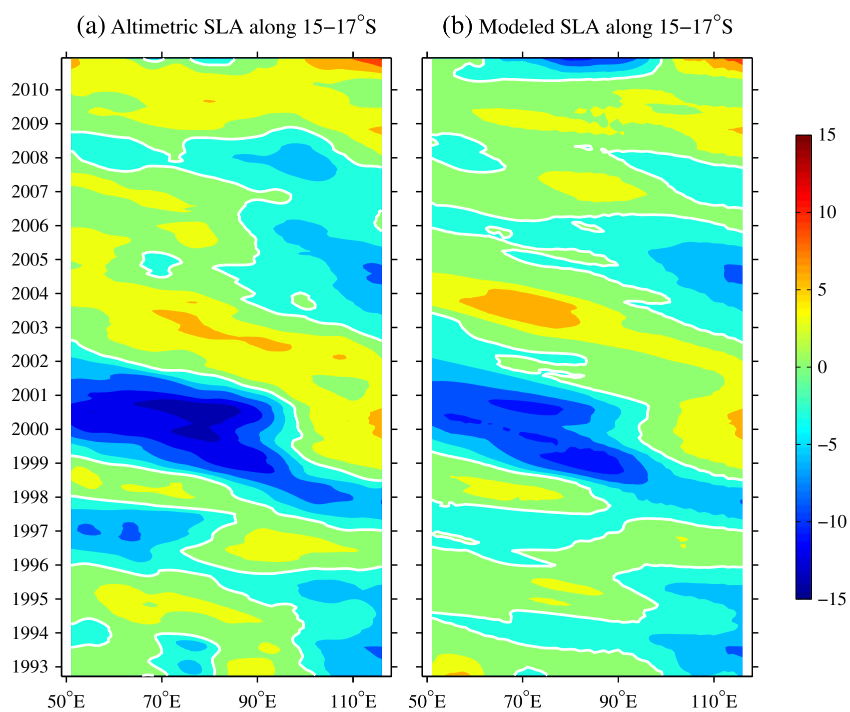


**Figure 7.** Time-longitude plot of the low-frequency (with period > 13 month) SSH anomalies along the 15°S–17°S band from (a) the satellite altimeter measurements, and (b) the wind-forced baroclinic Rossby wave model.

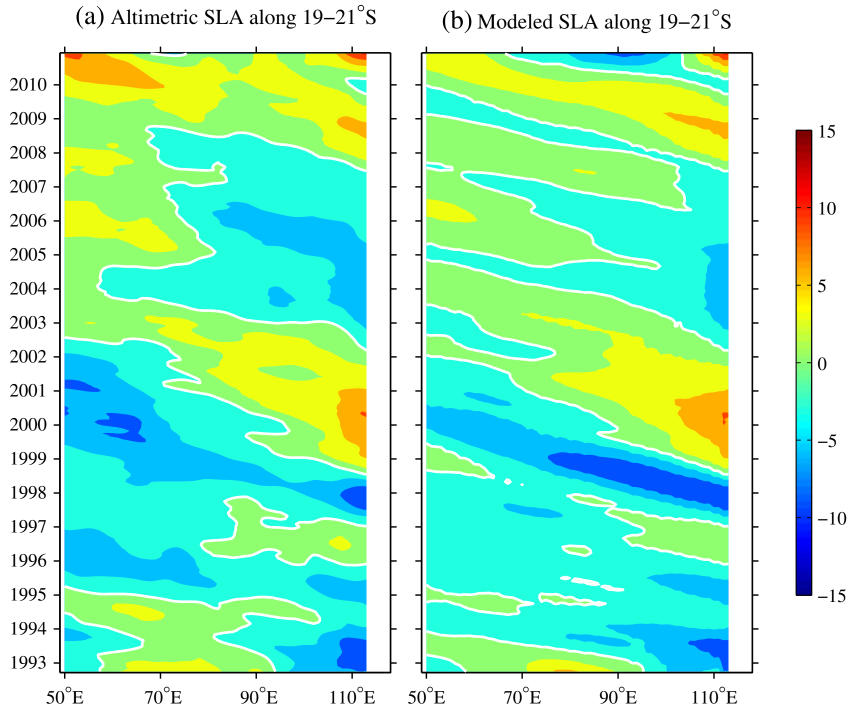


**Figure 8.** Time-longitude plot of the low-frequency (with period > 13 month) SSH anomalies along the 19°S–21°S band from (a) the satellite altimeter measurements, and (b) the wind-forced baroclinic Rossby wave model.

eastern boundary, and $h_I(X,y_0,t)$ represents the SLA driven by the SIO WSC west of longitude X.

$$H_w(t) = h(x_w, y_0, t), \tag{4}$$

$$h_I(X, y_0, t) = \frac{1}{\rho_0 g f} \int_X^{x_w} \frac{g'}{c_R} \nabla \times \tau\left(x', y_0, t + \frac{x_w - x'}{c_R}\right) \exp\left[\frac{\varepsilon}{c_R}\left(x_w - x'\right)\right] dx'. \tag{5}$$

[23] Here we focus on the low-frequency variability, which is of the interest of this study. Meanwhile, to examine the reliability of the estimated explained variance, S($X$) is calculated under different ε.

[24] The S($X$) in Figure 9a reveals that much of the low-frequency $H_W$ variance in the northwestern box is caused by the interior wind forcing west of 95°E. With the dissipation timescale $\varepsilon^{-1}$ varying from 0.5 to 4 yr, the contributions of southern IO WSC always exceed 81% of the total explained variance by both remote and IO forcing. Even without dissipation, the WSC west of 95°E could still explain more than 60% of the $H_W$ variance, while the remote forcing from the Pacific has minor influence. As indicated in Figure 9b, the local wind forcing also plays an important role in modulating the low-frequency $H_W$ variability at 15°S–17°S, with the explained variance always larger than 48% under different ε. With a reasonable $\varepsilon^{-1}$ ranging from 2 to 4 yrs, the zonal distributions of S($X$) are similar and the contributions of SIO wind forcing are always larger than 76%, corroborating the dominance of SIO WSC forcing, which is similar to the cause of interannual SSH variability around the thermocline ridge [*Trenary and Han*, 2012]. The most important contributor of $H_W$ is the WSC between 70°E and 95°E, where the strong WSC variability, as shown in EOF-1 pattern (Figure 5), explains about 70% of the $H_W$ variance. While the dominating effect of SIO wind has been proposed and recognized before [*Birol and Morrow*, 2001; *Wijffels and Meyers*, 2004], we have further identified that the $H_W$ to the north of 18°S is primarily caused by westward-propagating Rossby waves forced by WSC in 70°E–95°E, instead of local wind-driven Ekman pumping in the western basin (50°E–70°E).

[25] As can be seen in Figure 9c, the S($X$) in the southwestern box is more sensitive to ε than those in the northern two boxes. With the $\varepsilon^{-1}$ varying from 4 to 2 yrs, the local wind-driven signals explain 3%–65% of the low-frequency $H_w$ variance. With the optimal $\varepsilon^{-1} \sim 3$ yr, the local WSC forcing explains 28% of the low-frequency $H_w$ variance, which is much lower than the values in the northern part and indicates that the remote Pacific forcing exerts stronger influence on the modeled $H_W$ at this latitudinal band. As indicated in Figure 4a, the Rossby waves radiated from the eastern boundary have relatively large amplitude at ~20°S, whereas the low-frequency WSC variability around 20°S is much weaker than that to the north of 18°S (Figure 5), leading to smaller SLA amplitude (Figures 6c and 8) and lesser contribution by local WSC to the modeled $H_W$ (Figure 9c). Thus, the remote signals from the Pacific radiated from the eastern boundary are likely having relatively more contributions at this latitude.

## 4. The Oceanic Variability in the ORA-S3 Model

[26] In this section, the three-dimensional model outputs from the ECMWF ORA-S3 are utilized to further investigate the oceanic vertical structure associated with the SLA variability. We mainly focus on two issues: one is the respective

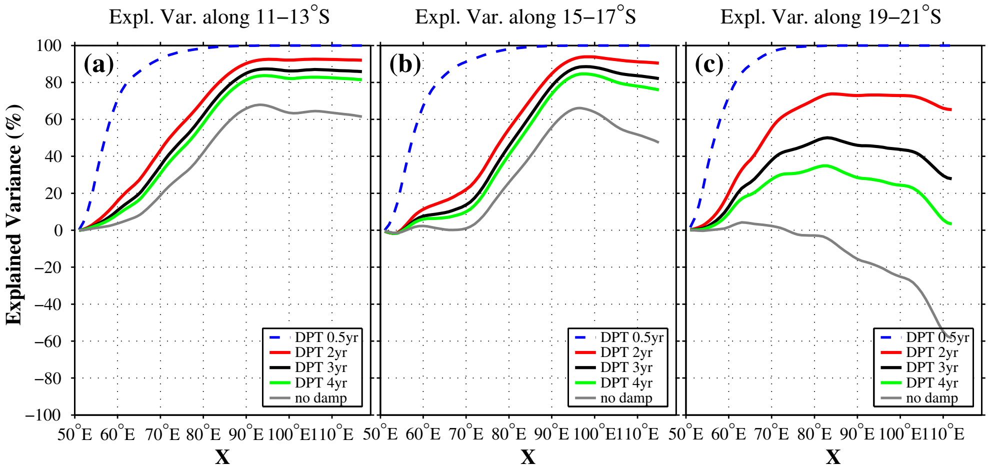


**Figure 9.** The percentage of explained variance of the modeled low-frequency $H_W$ signals (with period > 13 month) by the cumulative wind forcing from 51°E to longitude X. The $H_w$ is averaged within (a) northwestern box; (b) middle-west box; and (c) southwestern box. The boxes are shown in Figure 1b.

contributions of mass and steric components to the sea level rise in the western SIO; the other is the relationship between sea level variability and the oceanic meridional transports at the thermocline depth.

### 4.1. ECMWF ORA-S3 Model Validations

[27] Before exploring the ocean processes related to SSH changes, we first verify the model's performance in the SIO by comparing it with satellite altimeter observations. It could be seen in Figure 1c that the simulated mean geostrophic circulation inferred from the mean SSH pattern resembles the altimetry observations (Figure 1b). Between 10°S and 30°S, the subtropical gyre, as well as the SEC, SICC, and Southeast Madagascar Current, is well reproduced by the ORA-S3. Meanwhile, the ORA-S3 also captures the large-scale pattern of observed SSH trend, probably because the model assimilates global sea level trend [*Balmaseda et al*., 2008]. The observed and simulated SSH trends within 10°–30°S are at 5.1 and 6.1 mm/yr, respectively. To the east of Madagascar coast, the largest SSH rise occurs around 20°–25°S. Note that the coarse model resolution of the ORA-S3 limits the simulations of mesoscale structures as in the altimeter observations.

[28] To examine the simulated SSH in the ORA-S3 in more detail, we plot in Figure 10 the observed and modeled low-frequency SLA time series within the six boxes near the east and west coasts. In all these boxes, the observed and modeled SSH anomalies are highly correlated, demonstrating

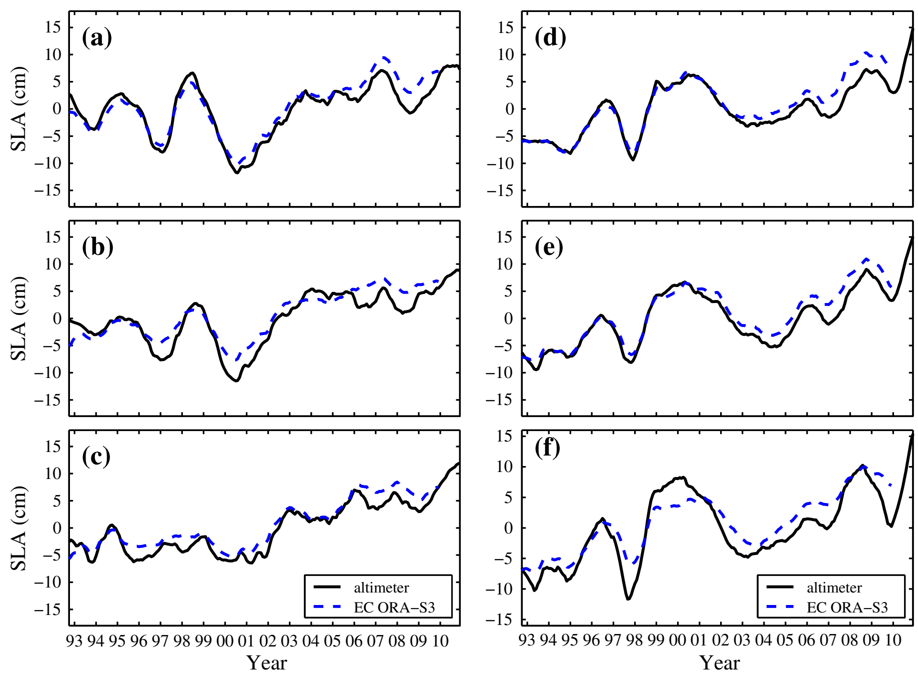


**Figure 10.** Low-frequency SSH variability (with period > 13 month) from altimetric observation (solid line) and ORA-S3 (dashed line) in the (a) northwestern box, (b) middle-west box, (c) southwestern box, (d) northeastern box, (e) middle-east box, and (f) southeastern box. The boxes are shown in Figure 1b.

that ORA-S3 is able to simulate both the observed SSH trends and low-frequency fluctuations. Besides, the performances of ORA-S3 had also been validated in other works [e.g., *Balmaseda et al*., 2008; *Lee et al*., 2010]. For example, *Lee et al*. [2010] compared the volume transports of ITF from 14 data-assimilation models including ORA-S3 and validated the consistency of the ORA-S3 simulations with the in situ observations. The observation-model agreement makes it feasible to utilize the ORA-S3 to study the variations of 3-D ocean structure related to the SSH changes in the SIO.

### 4.2. Temperature and Salinity Changes Associated With the Trend in $H_W$

[29] In both the altimeter and ORA-S3 results, the linear rise trends of $H_E$ and $H_W$ (see Figures 1b, 1c, and 10) are above the 95% confidence level, as evaluated from the bootstrap method. To illustrate the internal structures associated with the significant SSH rise near the western SIO basin, Figures 11a and 11b show the linear trends in the ORA-S3 temperature and salinity transects along 55°E during 1993–2009. To the south of 10°S, broad-scale warming trend >0.02 °C/yr appears mostly in the upper 100 m above the 20 °C isotherm. Only at 20°–25°S, around the center of subtropical gyre, the warming signal extends from the surface to the 14 °C isotherm at about 400 m depth. In contrast to the temperature trend, the salinity trend exhibits a more inhomogeneous spatial pattern: surface freshening and salinification mainly appears south and north of 10°S, respectively, and the subsurface salinification trend occurs at 150–400 m depth south of 20°S and at ~200 m depth in 10°–15°S.

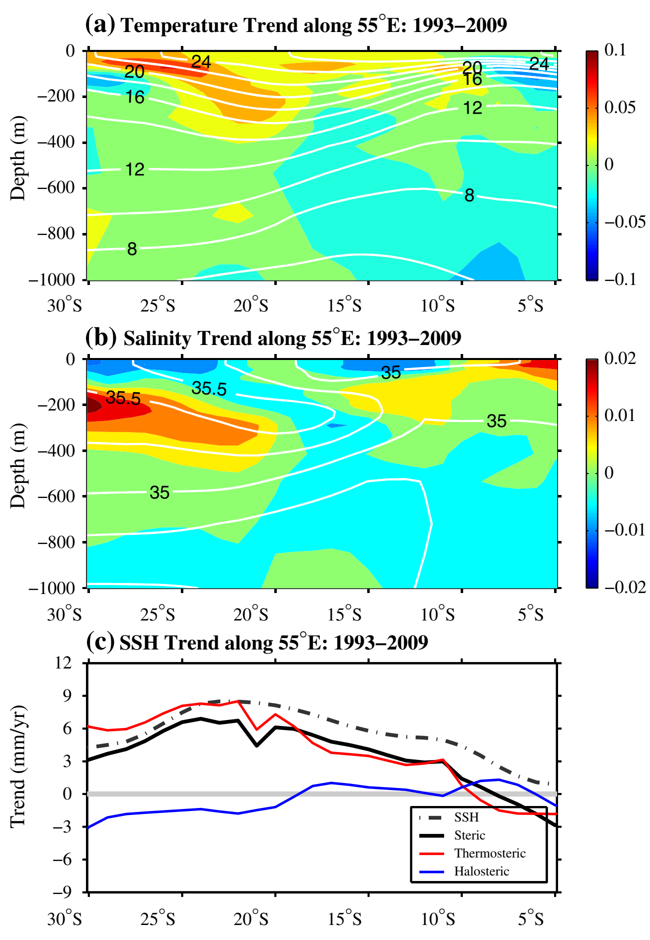


**Figure 11.** (a) Linear trend in temperature (color shading) as a function of depth and latitude along 55°E over the 1993–2009 period. Contours show the mean temperature distribution of 1993–2009. (b) As in (a), but for the salinity field. (c) Total and steric SSH trends (black dash and black solid lines) along 55°E over the 1993–2009 period. The red (blue) line denotes the thermosteric (halosteric) component of the steric SSH trend.

[30] The SSH variability is mainly attributed to the steric and mass-induced components [*Gill and Niiler*, 1973]. To quantify the relative contribution of temperature and salinity to the steric sea level trend, we estimate the thermosteric and halosteric SSH components by replacing the time-varying $S(x,y,z,t)$ and $T(x,y,z,t)$ with their time-mean values $\bar{S}(x,y,z)$ and $\bar{T}(x,y,z)$ during 1993–2009. As shown in Figure 11c, the steric sea level trend along 55°E peaks at 20°–25°S, consistent with the total SSH trend, and is largely determined by the thermosteric component. There is a negative contribution from the halosteric component south of 20°S, likely due to the salinification trend in the thermocline. It is worth emphasizing that the mean steric SSH trend between 10° and 30°S (4.9 mm/yr) is less than the total SSH trend (6.6 mm/yr), and their difference may reflect the contribution of bottom pressure associated with the mass changes [*Gill and Niiler*, 1973] or deep ocean warming which may not be properly considered by the data-assimilation process because of fewer observations. Due to the sparseness of in situ observational data over the SIO region [*Harrison and Carson*, 2007], more observational and modeling efforts are needed to further validate the above phenomena and clarify the underlying dynamics associated with the local SSH trend.

### 4.3. The Linkage Between SLA and Meridional Transport in ORA-S3

[31] In the IO, 15°S is regarded as the key transect where the meridional transports are often used to measure the STC variability [*Schott et al*., 2004; *Trenary and Han*, 2008]. From geostrophy, *Lee and McPhaden* [2008] suggested that variability of pycnocline transport could be inferred from the SSH difference across the SIO basin. To verify the relationship between the oceanic transports and the sea level variations, we estimate the meridional transports across the surface and subsurface layers across the 15°S transect, as well as the ITF transports across 114°E, during 1959–2009. Both the surface and subsurface layers are defined by the STC density ranges similar to *Trenary and Han* [2008] and *Schott et al*. [2008]. The surface layer ranges from the sea surface to the mixed layer depth or the 22.5 kgm$^{-3}$ isopycnal layer, depending on which one is deeper. The lower layer is defined as a layer between the bottom of the surface layer and the 26.2 kgm$^{-3}$ isopycnal layer (Figure 12). The transports in surface and lower layers of 15°S transect are derived from the cross-basin zonal integrations of meridional transports within their respective depth ranges. The transports contributed from the interior and western boundary current (WBC) are separated at 56°E according to the model's meridional velocity pattern along the 15°S transect. In the SIO open ocean, the surface layer is dominated by the poleward mean flow with the transport of -13.0 ± 1.2 Sv. It is partly

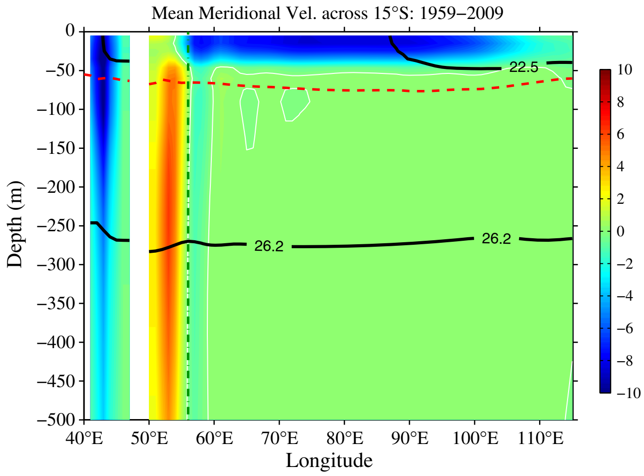


**Figure 12.** Mean meridional velocity at the 15°S transect during 1959–2009 derived from ORA-S3, with isopycnals (black, kg/m$^3$) marking the upper and lower boundaries of the STC layers. Red dashed line represents the bottom of the mixed layer, and the green line separates the interior and western boundary.

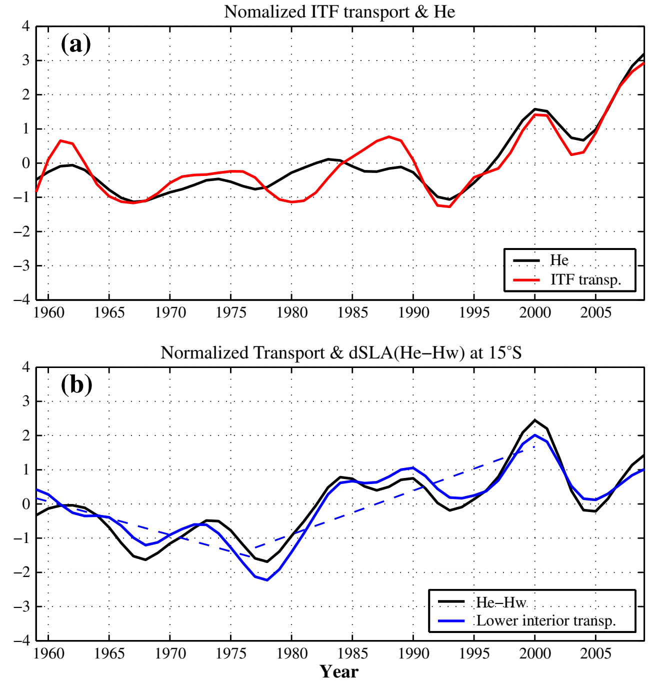


**Figure 13.** (a) The normalized $H_E$ at 15°S (black line) and the normalized reversed ITF transport across 114°E (red line). (b) The normalized SLA difference ($H_E$ – $H_W$) between 115°E–120°E and 50°E–55°E along 15°S (black line) and the normalized reversed transport for the lower interior (blue solid line). The blue dashed lines in Figure 13b indicate the linear trends of reversed interior transport in the lower layer during 1959–1977 and 1977–2000.

compensated by the equatorward lower layer mean transports of 7.1 ± 0.9 Sv, to which the interior flow and WBC contribute 2.2 ± 1.9 Sv and 4.9 ± 1.6 Sv, respectively. Toward the west, there exists a vertically uniformed southward flow in the Mozambique Channel with the transports of -2.3 ± 0.4 Sv and -4.7 ± 0.5 Sv in the surface and lower layers, respectively. A large portion of the net transports across 15°S is attributed to the ITF north of 15°S, which flows westward at -11.8 ± 0.7 Sv within the STC density range, supplies the SEC and the Leeuwin Current, and eventually exits the IO with the southward currents. The transports of these branches are summarized in Table 1.

[32] To examine the correspondence of the SIO transports with the sea level variability, we further compare the SLA and transport anomalies based on the ORA-S3 data. As the STC is considered to be quasi-steady on decadal or longer timescales [e.g., *McCreary and Lu*, 1994; *McPhaden and Zhang*, 2004], a 7 year Hanning filter is applied to the SLAs and transports to remove interannual variations. For easy viewing, the low-pass filtered SLA and transport anomalies are normalized, and then, the transport anomalies are reversed in Figure 13, that is, the westward ITF and southward meridional transports are defined as positive.

[33] As shown in Figure 13a, the simulated ITF generally captures the observed low-frequency variations, especially the increasing trends during 1993–2000 [*Lee et al.*, 2010] and 1993–2009 [*Feng et al.*, 2011] associated with the strengthening tropical Pacific trade winds. Figure 13a also elucidates that the time series of ITF transport across 114°E resembles the normalized $H_E$ at 15°S remarkably well, indicating strong association between ITF and $H_E$. The linear regression between them suggests that the $H_E$ could explain 82.5% of the ITF variance, and the regression coefficient is 0.19 Sv per cm sea level anomaly. The most prominent increasing trends of ITF and $H_E$ occur during the altimetric epoch of 1993–2009.

[34] Similarly, Figure 13b shows the normalized interior transport anomalies in the lower layer of the interior ocean, together with the normalized zonal SSH difference ($H_E$ - $H_W$) at 15°S. The $H_E$ and $H_W$ are averaged within 115°–120°E and 50°–55°E, the same as the boxes shown in Figure 1b. It can be clearly seen that the SSH difference across the SIO basin is closely correlated with the interior transport in the lower layer. According to the linear regression analysis, the cross-basin SSH difference explains 88.8% of the interior transport variance within the lower layer and the regression coefficient is 0.31 Sv per cm sea level difference. Associated with the sea level difference across the SIO basin, the interior transport in the lower layer shows an equatorward increasing trend (0.12 Sv/yr) during 1959–1977 and a decreasing trend (-0.14 Sv/yr) during

**Table 1.** Meridional Transports of STC Branches Across the 15°S Transect and the Westward ITF Transports Across the 114°E Transect[a]

| | Interior | WBC | Mozambique Channel | Total | ITF |
|---|---|---|---|---|---|
| Surface Layer | −13.6 ± 1.8 | 0.6 ± 0.8 | −2.3 ± 0.4 | −15.3 ± 1.1 | −5.1 ± 0.8 |
| Lower Layer | 2.2 ± 1.9 | 4.9 ± 1.6 | −4.7 ± 0.5 | 2.4 ± 0.7 | −6.7 ± 1.0 |

[a]The standard deviations of low-frequency transports variations (with period > 13 months) are also listed.

1977–2000 (Figure 13b). A close examination at the most recent decade indicates that the transport rebounds during 2000–2004 and decrease slowly afterward, consistent with the observed $H_E$ - $H_W$. Note that the $H_E$ and $H_W$ individually could explain 34.9% and 28.3% of the interior transport variance. Thus, although previous studies [e.g., *Lee and McPhaden*, 2008] suggest the dominance of $H_E$ to the cross-basin SSH difference and associated lower branch transports, the results based on ORA-S3 indicate that variability of $H_W$ is of equally importance.

## 5. Summary and Discussions

[35] Using multi-satellite altimetry measurements in the 1993–2010 period, this study examines the SSH variability in the SIO. Particular attention is paid to the low-frequency SSH changes near the western boundary of the basin ($H_W$). A 1½-layer reduced-gravity model is used to isolate the role of linear wind driven processes in driving sea level variations. The model, which reflects the first-mode baroclinic Rossby wave dynamics, includes the responses forced by the WSC in interior SIO and the SSH changes along the eastern boundary. The data-model comparisons demonstrate that the model, though simple in its formulation, contains the essential dynamics that can explain many of the observed SSH variations.

[36] North of the SEC bifurcation latitude, low-frequency sea level variability exhibits large amplitudes on interannual-decadal timescales, primarily driven by local WSC, with a minor influence from the Pacific through the wave guide across the Indonesian Seas. In contrast, the variability around 20ºS displays lower amplitudes due to weaker wind variations at this latitude band, whereas the regional sea level exhibits the largest rise trend in the 1993–2010 period. The Rossby waves generated at the eastern boundary at ~20ºS have relatively large amplitudes and may play a relatively more important role in modulating the sea level variations in the western basin. The relatively low predictive skill of the model at ~20ºS suggests that the baroclinic Rossby wave model is less successful to capture the sea level dynamics in this region where the low-frequency WSC forcing is relatively weak. To better understand the sea level variability around 20ºS, the influences of other factors deserve further investigation under a more complete dynamic framework. South of 23ºS, the Leeuwin Current prohibits the westward propagation of coastal signals [*Clarke and Li*, 2004]. Meanwhile, there exists strong eddy variability in the interior basin induced by the baroclinic instability of the SICC [e.g., *Jia et al*., 2011], which reduces the predictive skill of the linear Rossby wave model south of 23ºS to a certain degree.

[37] As the SIO is directly forced by the strong seasonal monsoons, the baroclinic Rossby wave model could largely capture the seasonal SSH signals. This is different from the extra-equatorial Southern Pacific Ocean, where, though the interannual-decadal variability could be explained by the baroclinic Rossby wave dynamics, the seasonal SSH signal is dominated by the surface heating and barotropic Sverdrup response to the wind forcing [*Vivier et al*., 1999; *Bowen et al*., 2006].

[38] The ECMWF ORA-S3 model captures the observed SSH increasing trend and low-frequency variability in the SIO. Along the 55ºE transect, the ORA-S3 suggests that the thermosteric signals contribute dominantly to the steric sea level rise, which explains most of the total SSH rise. The broad-scale warming, which can be induced by both the wind-driven thermocline deepening [*Han et al*., 2010; *Timmermann et al*., 2010] and/or the thermal expansion of the warming ocean [*Bindoff et al*., 2007], mainly occurs in the upper 100 m depth of the extra-equatorial region and could only reach 400 m depth at 20ºS–25ºS, leading to the local maximum of SSH rise. Because the salinity fields in the western SIO do not vary monotonically with depth, the salinity trends are vertically incoherent and the resultant halosteric SSH signals have little impact on the regional $H_W$ trend.

[39] The close relationships between the decadal sea level variations and oceanic transports are identified in the ORA-S3. Sea level variations in the eastern SIO well indicate the changes of ITF transport, in accordance with the previous observational evidence [e.g., *Feng et al*., 2010, 2011]. At 15ºS, the interior meridional transport within the pycnocline layer, which contributes significantly to the lower branch of STC, could be generally explained by the cross-basin sea level difference ($H_E$ - $H_W$), instead of solely by $H_E$ or $H_W$. In summary, the strength of the meridional overturning circulation in the SIO, which is highly related to the cross-basin sea level difference at 15°S, is predominantly influenced by both remote wind forcing in the tropical Pacific, which drives the $H_E$ variability, and local SIO wind forcing, which to a large extent controls the $H_W$ variability.

[40] **Acknowledgments.** This study benefits from discussions with Profs. Bo Qiu and Shang-Ping Xie. We are also grateful to the two anonymous reviewers whose constructive comments helped improve the manuscript. The ECMWF ORA-S3 data were provided by Magdelena Balmaseda and Jim Potemra via the Asia-Pacific Data Research Center, University of Hawaii. The merged satellite altimeter data were provided by the CLS Space Oceanography Division. W.Z. and Y.D. are supported by National Basic Research Program of China (2010CB950302, 2012CB955603), National Natural Science Foundation of China (41176028, 41176024). M.F. and A.S are supported by CSIRO Wealth from Oceans Flagship.

## References

Alory, G., S. Wijffels, and G. Meyers (2007), Observed temperature trends in the Indian Ocean over 1960–1999 and associated mechanisms, *Geophys. Res. Lett.*, *34*, L02606, doi:10.1029/2006GL028044.

Bader, J., and M. Latif (2003), The impact of decadal-scale Indian Ocean sea surface temperature anomalies on Sahelian rainfall and the North Atlantic Oscillation, *Geophys. Res. Lett.*, *30*(22), 2169, doi:10.1029/2003GL018426.

Balmaseda, M. A., A. Vidard, and D. L. T. Anderson (2008), The ECMWF Ocean Analysis System: ORA-S3, *Mon. Weather Rev.*, *136*, 3018–3034.

Bindoff, N. L., et al. (2007), Observations: Oceanic climate change and sea level, in *Climate Change 2007: The Physical Science Basis*, edited by S. Solomon et al., pp. 385–432, Cambridge Univ. Press, Cambridge, U. K.

Birol, F., and R. Morrow (2001), Sources of the baroclinic waves in the southeast Indian Ocean, *J. Geophys. Res.*, *106*, 9145–9160.

Bowen, M. M., P. J. H. Sutton, and D. Roemmich (2006), Wind-driven and steric fluctuations of sea surface height in the southwest Pacific, *Geophys. Res. Lett.*, *33*, L14617, doi:10.1029/2006GL026160.

Capotondi, A., and M. A. Alexander (2001), Rossby waves in the tropical North Pacific and their role in decadal thermocline variability, *J. Phys. Oceanogr.*, *31*, 3496–3515.

Chambers, D. P., B. D. Tapley, and R. H. Stewart (1999), Anomalous warming in the Indian Ocean coincident with El Niño, *J. Geophys. Res.*, *104*, 3035–3047.

Chelton, D. B., R. A. de Szoeke, M. G. Schlax, K. E. Naggar, and N. Siwertz (1998), Geographical variability of the first baroclinic Rossby radius of deformation, *J. Phys. Oceanogr.*, *28*, 433–460.

Church, J. A., N. J. White, R. Coleman, K. Lambeck, and J. X. Mitrovica (2004), Estimates of the regional distribution of sea-level rise over the 1950 to 2000 period, *J. Clim.*, *17*, 2609–2625.

Clarke, A. J., and J. Li (2004), El Niño/La Niña shelf edge flow and Australian western rock lobsters, *Geophys. Res. Lett.*, *31*, L11301, doi:10.1029/2003GL018900.
Du, Y., and T. Qu (2010), Three inflow pathways of the Indonesian throughflow as seen from the simple ocean data assimilation, *Dyn. Atmos. Oceans*, doi:10.1016/j.dynatmoce.2010.04.001.
Du, Y., and S.-P. Xie (2008), Role of atmospheric adjustments in the tropical Indian Ocean warming during the 20th century in climate models, *Geophys. Res. Lett.*, *35*, L08712, doi:10.1029/2008GL033631.
Du, Y., S.-P. Xie, K. Hu, and G. Huang (2009), Role of Air–Sea Interaction in the Long Persistence of El Niño–Induced North Indian Ocean Warming, *J. Climate*, *22*, 2023–2038.
Ducet, N., P.-Y. Le Traon, and G. Reverdin (2000), Global high-resolution mapping of ocean circulation from TOPEX/Poseidon and ERS-1 and -2, *J. Geophys. Res.*, *105*, 19 477–19 498.
Feng, M., C. Boning, A. Biastoch, E. Behrens, E. Weller, and Y. Masumoto (2011), The reversal of the multi-decadal trends of the equatorial Pacific easterly winds, and the Indonesian Throughflow and Leeuwin Current transports, *Geophys. Res. Lett.*, *38*, L11604, doi:10.1029/2011GL047291.
Feng, M., M. J. McPhaden, and T. Lee (2010), Decadal variability of the Pacific subtropical cells and their influence on the southeast Indian Ocean, *Geophys. Res. Lett.*, *37*, L09606, doi:10.1029/2010GL042796.
Feng, M., Y. Li, and G. Meyers (2004), Multidecadal variations of Fremantle sea level: Footprint of climate variability in the tropical Pacific, *Geophys. Res. Lett.*, *31*(16), L16302, doi:10.1029/2004GL019947.
Gill, A., and P. Niiler (1973), The theory of the seasonal variability in the ocean, *Deep Sea Res.*, *20*, 141–177.
Gordon, A. L., and R. A. Fine (1996), Pathways of the water between the Pacific and Indian Oceans in the Indonesian seas, *Nature*, *379*, 146–149.
Han, W., G. A. Meehl, and A. Hu (2006), Interpretation of tropical thermocline cooling in the Indian and Pacific oceans during recent decades, *Geophys. Res. Lett.*, *33*, L23615, doi:10.1029/2006GL027982.
Han, W., et al. (2010), Patterns of Indian Ocean sea level change in a warming climate, *Nat. Geosci.*, doi:10.1038/NGEO901.
Harrison, D. E., and M. Carson (2007), Is the world ocean warming? Upper ocean trends, 1950–2000, *J. Phys. Oceanogr.*, *37*, 174–187.
Hoerling, M., J. W. Hurrell, T. Xu, G. T. Bates, and A. S. Phillips (2004), Twentieth century North Atlantic climate change. Part II: Understanding the effect of Indian Ocean warming, *Clim. Dyn.*, *23*, 391–405.
Jia, F., L. Wu, J. Lan, and B. Qiu (2011), Interannual modulation of eddy kinetic energy in the southeast Indian Ocean by Southern Annular Mode, *J. Geophys. Res.*, *116*, C02029, doi:10.1029/2010JC006699.
Kessler, W. S., and J. P. McCreary (1993), The annual wind-driven Rossby wave in the subthermocline equatorial Pacific, *J. Phys. Oceanogr.*, *23*, 1192–1207.
Lee, T. (2004), Decadal weakening of the shallow overturning circulation in the south Indian Ocean, *Geophys. Res. Lett.*, *31*, L18305, doi:10.1029/2004GL020884.
Lee, T., et al. (2010), Consistency and fidelity of Indonesian-throughflow total volume transport estimated by 14 ocean data assimilation products, *Dyn. Atmos. Oceans*, *50*(2), 201–223.
Lee, T., and J. Marotzke (1998), Seasonal cycle of meridional overturning and heat transport of the Indian Ocean, *J. Phys. Oceanogr.*, *28*, 923–943.
Lee, T., and M. J. McPhaden (2008), Decadal phase change in large-scale sea level and winds in the Indo-Pacific region at the end of the 20th century, *Geophys. Res. Lett.*, *35*, L01605, doi:10.1029/2007GL032419.
Masumoto, Y., and G. Meyers (1998), Forced Rossby waves in the southern tropical Indian Ocean, *J. Geophys. Res.*, *103*, 27589–27602.
McCreary, J. P., Jr., P. K. Kundu, and R. L. Molinari (1993), A numerical investigation of dynamics, thermodynamics and mixed-layer processes in the Indian Ocean, *Prog. Oceanogr.*, *31*, 181–244.
McCreary, J. P., and P. Lu (1994), Interaction between the subtropical and equatorial ocean circulations: The subtropical cell, *J. Phys. Oceanogr.*, *24*, 466–497.
McPhaden, M. J., and D. Zhang (2004), Pacific Ocean circulation rebounds, *Geophys. Res. Lett.*, *31*, L18301, doi:10.1029/2004GL020727.
Meyers, G. (1979), On the annual Rossby wave in the tropical North Pacific Ocean, *J. Phys. Oceanogr.*, *9*, 663–674.
Morrow, R., F. Fang, M. Fieux, and R. Molcard (2003), Anatomy of three warm-core Leeuwin Current eddies, *Deep Sea Res.*, *50*, 2229–2243, doi:10.1016/S0967-0645(03)00054-7.
Potemra, J. T. (2001), Contribution of equatorial Pacific winds to southern tropical Indian Ocean Rossby waves, *J. Geophys. Res.*, *106*, 2407–2422.
Qiu, B. (2002), Large-scale variability in the midlatitude subtropical and subpolar North Pacific Ocean: Observations and causes, *J. Phys. Oceanogr.*, *32*, 353–375.
Qiu, B., and S. Chen (2010), Interannual-to-decadal variability in the bifurcation of the North Equatorial Current off the Philippines, *J. Phys. Oceanogr.*, *40*, 2525–2538.
Qu, T., and G. Meyers (2005), Seasonal Characteristics of Circulation in the Southeastern Tropical Indian Ocean, *J. Phys. Oceanogr.*, *35*, 255–267.
Quartly, G. D., J. J. H. Buck, M. A. Srokosz, and A. C. Coward (2006), Eddies around Madagascar—The retroflection re-considered, *J. Mar. Syst.*, *63*(3–4), 115–129, doi:10.1016/j.jmarsys.2006.06.001.
Rennie, S. J., C. B. Pattiaratchi, and R. D. McCauley (2007), Eddy formation through the interaction between the Leeuwin Current, Leeuwin Undercurrent and topography, *Deep Sea Res., Part II*, *54*, 818–836, doi:10.1016/j.dsr2.2007.02.005.
Rio, M. H., S. Guinehut, and G. Larnicol (2011), New CNESCLS09 global mean dynamic topography computed from the combination of GRACE data, altimetry, and in situ measurements, *J. Geophys. Res.*, *116*, C07018, doi:10.1029/2010JC006505.
Schott, F., and J. P. McCreary (2001), The monsoon circulation of the Indian Ocean, *Prog. Oceanogr.*, *51*, 1–123.
Schott, F., J. P. McCreary, and G. C. Johnson (2004), Shallow overturning circulations of the tropical-subtropical oceans, in *Earth's Climate: The Ocean-Atmosphere Interaction*, Geophys. Monogr. Ser., vol. 147, edited by C. Wang, S.-P. Xie, and J. A. Carton, pp. 261–304, AGU, Washington, D. C.
Schott, F. A., L. Stramma, W. Wang, B. S. Giese, and R. Zantopp (2008), Pacific Subtropical Cell variability in the SODA 2.0.2/3 assimilation, *Geophys. Res. Lett.*, *35*, L10607, doi:10.1029/2008GL033757.
Schott, F. A., S.-P. Xie, and J. P. McCreary Jr. (2009), Indian Ocean circulation and climate variability, *Rev. Geophys.*, *47*, RG1002, doi:10.1029/2007RG000245.
Schwarzkopf, F. U., and C. W. Böning (2011), Contribution of Pacific wind stress to multi-decadal variations in upperocean heat content and sea level in the tropical south Indian Ocean, *Geophys. Res. Lett.*, *38*, L12602, doi:10.1029/2011GL047651.
Timmermann, A., S. McGregor, and F.-F. Jin (2010), Wind effects on the past and future regional sea level trends in the southern Indo-Pacific, *J. Climate*, *23*, 4429–4437.
Trenary, L. L., and W. Han (2008), Causes of decadal subsurface cooling in the tropical Indian Ocean during 1961–2000, *Geophys. Res. Lett.*, *35*, L17602, doi:10.1029/2008GL034687.
Trenary, L. L., and W. Han (2012), Intraseasonal-to-Interannual Variability of South Indian Ocean Sea Level and Thermocline: Remote versus Local Forcing, *J. Phys. Oceanogr.*, *42*, 602–627.
Verschell, M. A., J. C. Kindle, and J. J. O'Brien (1995), Effects of Indo–Pacific throughflow on the upper tropical Pacific and Indian Oceans, *J. Geophys. Res.*, *100*, 18409–18420.
Vivier, F., K. A. Kelly, and L. Thompson (1999), Contributions of wind forcing, waves, and surface heating to sea surface height observations in the Pacific Ocean, *J. Geophys. Res.*, *104*, 20,767–20,788.
Wijffels, S., and G. Meyers (2004), An Intersection of Oceanic Waveguides: Variability in the Indonesian Throughflow Region, *J. Phys. Oceanogr.*, *34*, 1232–1253.
Wolff, J., E. Maier-Reimer, and S. Legutke (1997), The Hamburg Ocean Primitive Equation model. Deutsches Klimarechenzentrum Tech. Rep. 13, Hamburg, Germany, 98 pp.
Xie, S.-P., H. Annamalai, F. A. Schott, and J. P. McCreary (2002), Structure and mechanisms of South Indian Ocean climate variability, *J. Climate*, *15*, 864–878.
Xie, S.-P., K. Hu, J. Hafner, H. Tokinaga, Y. Du, G. Huang, and T. Sampe (2009), Indian Ocean capacitor effect on Indo-western Pacific climate during the summer following El Nino, *J. Climate*, *22*, 730–747.
Yokoi, T., T. Tozuka, and T. Yamagata (2008), Seasonal Variation of the Seychelles Dome, *J. Climate*, *21*, 3740–3754, doi: 10.1175/2008JCLI1957.1.
Yu, W., B. Xiang, L. Liu, and N. Liu (2005), Understanding the origins of interannual thermocline variations in the tropical Indian Ocean, *Geophys. Res. Lett.*, *32*, L24706, doi:10.1029/2005GL024327.
Zhou, L., R. Murtugudde, M. Jochum (2008), Seasonal Influence of Indonesian Throughflow in the Southwestern Indian Ocean, *J. Phys. Oceanogr.*, *38*, 1529–1541.